Research Article

Cihyun Kim, Tae Jin Yoo, Min Gyu Kwon, Kyoung Eun Chang, Hyeon Jun Hwang
and Byoung Hun Lee*

High-performance near-infrared photodetectors based on gate-controlled graphene–germanium Schottky junction with split active junction

Abstract: The structure of a gate-controlled graphene/germanium hybrid photodetector was optimized by splitting the active region to achieve highly sensitive infrared detection capability. The strengthened internal electric field in the split active junctions enabled efficient collection of photocarriers, resulting in a responsivity of 2.02 A W^{-1} and a specific detectivity of 5.28×10^{10} Jones with reduced dark current and improved external quantum efficiency; these results are more than doubled compared with the responsivity of 0.85 A W^{-1} and detectivity of 1.69×10^{10} Jones for a single active junction device. The responsivity of the optimized structure is 1.7, 2.7, and 39 times higher than that of previously reported graphene/Ge with Al_2O_3 interfacial layer, gate-controlled graphene/Ge, and simple graphene/Ge heterostructure photodetectors, respectively.

1 Introduction

Various graphene/semiconductor Schottky junction photodetectors have been investigated to combine the benefits of graphene and semiconductors in terms of photonic responses [1–12]. In particular, graphene/Ge heterojunctions have been used in infrared wavelength regions owing to their simple structure, exceptional optoelectronic properties, and direct compatibility with high-speed integrated circuits [13–15].

Zeng et al. demonstrated a graphene/Ge Schottky junction-based infrared photodetector with a responsivity of 51.8 mA W^{-1} operating at zero bias voltage [13]. Chang et al. reported a gate-modulated graphene/Ge Schottky junction photodetector with a responsivity of 750 mA W^{-1}. In this device, a self-amplification process is used to obtain a high photocurrent with a concurrent reduction in the dark current. The self-amplification mechanism is induced by asymmetric carrier transport and lifetime in the graphene and Ge regions [15]. Currently, the graphene/Ge junction photodetectors have a comparatively smaller gain than graphene/Si junction photodetectors, and the responsivity remains limited due to low external quantum efficiency (EQE) of 60% because of the long transit time of the minority carrier in the depletion region of Ge [12, 15]. These results suggest that a primary problem with a gate-controlled graphene/Ge Schottky junction photodetector is the inefficient transport of photogenerated carriers.

Recently, various approaches to improve carrier transport in graphene/semiconductor junctions through electric field engineering have been reported [16–25]. Bartolomeo et al. reported that a graphene/silicon-nanotip heterojunction creates a higher local electric field in the Si substrate, which improves the photo-charge separation [17]. Furthermore, several groups have investigated the spatial distribution of photocurrents in graphene/semiconductor heterojunctions to elucidate the mechanism of photocurrent transport using scanning photocurrent microscopy (SPCM). Unsuree et al. reported that the strong band bending of a silicon substrate induced by local strengthening of the electric field at the graphene edge influences the transit of photogenerated carriers in graphene/Si photodiodes [22]. Riazimehr et al. reported that the effective collection of

*Corresponding author: Byoung Hun Lee, Department of Electrical Engineering, Pohang University of Science and Technology, 77, Cheongam-ro, Nam-gu, Pohang-si, Gyeongsangbuk-do, 37673, Republic of Korea, E-mail: bhlee1@postech.ac.kr. https://orcid.org/0000-0002-4540-7731
Cihyun Kim, Tae Jin Yoo and Hyeon Jun Hwang, Department of Electrical Engineering, Pohang University of Science and Technology, 77, Cheongam-ro, Nam-gu, Pohang-si, Gyeongsangbuk-do, 37673, Republic of Korea. https://orcid.org/0000-0003-0396-2048 (C. Kim). https://orcid.org/0000-0003-3523-327X (T.J. Yoo)
Min Gyu Kwon and Kyoung Eun Chang, School of Materials Science and Engineering, Gwangju Institute of Science and Technology, 123, Cheomdangwagi-ro, Buk-gu, Gwangju, 61005, Republic of Korea

photogenerated carriers has been achieved with reduced surface recombination and an extended lifetime of minority carriers by inducing formation of an inversion layer in the adjacent graphene/SiO$_2$/Si structure [19, 21]. Although the interface between graphene and silicon may differ from that between graphene and germanium, these studies provide a suitable design guideline for graphene/Ge junction photodetectors.

In this study, gate-controlled hybrid infrared photodetectors with two different active regions, that is, a single active junction and a split active junction, were investigated. The split active junction structure was implemented to improve the EQE and reduce the dark current. The strengthened internal electric field enables photocarrier extraction with an internal gain, which was investigated using the SPCM and numerical simulation. As a result, a split active region improves the responsivity and specific detectivity to 2.02 A W^{-1} and 5.28 × 10^{10} Jones from 0.85 A W^{-1} and 1.69 × 10^{10} Jones for a single active device. This result is 1.7–39 times higher than the previously-reported responsivity of a graphene/Ge photodetector.

2 Experimental details

Figure 1A shows the fabricated devices with two different active regions, where the single active structure comprises only graphene/Ge

Schottky junctions, and the split active structure is divided into graphene/Ge regions and graphene/SiO$_2$/Ge regions. A cross-sectional schematic of the split active-junction device is shown in Figure 1B. The inset of Figure 1B is the equivalent circuit of the split active junction device comprising gate-controlled graphene/Ge Schottky diodes and graphene/SiO$_2$/Ge capacitors separated by an interdigitated insulating layer.

For device fabrication, a 100-nm-thick SiO$_2$ layer was deposited on an n-type Ge substrate (resistivity 2.5–2.7 Ω cm) using plasma-enhanced chemical vapor deposition (PECVD). The native oxide of the Ge could affect the interface quality; therefore, the substrate was immersed in deionized water at room temperature for 24 h to remove the native oxide; next, a 100-nm layer of SiO$_2$ was deposited on it [26, 27]. Thereafter, the SiO$_2$ layer was patterned to expose the Ge surface using photolithography and buffered oxide etching (BOE) process. Four types of devices with oxide widths of 0, 10, 20, and 30 μm were fabricated. Optical microscope images were obtained for the fabricated devices with oxide widths of 0 and 20 μm, as shown in Figure 1C.

Immediately afterward, a thermal CVD-grown monolayer graphene sheet was wet-transferred onto the patterned substrate using a polymethylmethacrylate (PMMA) sacrificial layer to minimize the amount of native oxide at the graphene/Ge interface. Following the transfer and acetone rinsing, graphene channel patterns were formed using 30-nm-thick Au as a hard mask and O$_2$-plasma etching. Raman spectra were obtained from graphene on SiO$_2$ and Ge substrates, as shown in Figure 1D. The quality of the graphene film was confirmed by the presence of a 2D band peak I_{2D} at 2680 cm^{-1}, G band peak I_G at 1580 cm^{-1}, and D band peak I_D at 1350 cm^{-1}. Furthermore, the 2D and G bands have an intensity ratio $I_{2D}/I_G > 2$, confirming that graphene is a monolayer.

Subsequently, a 100-nm-thick Au source electrode was formed on the graphene channel using an e-beam evaporator and photolithography
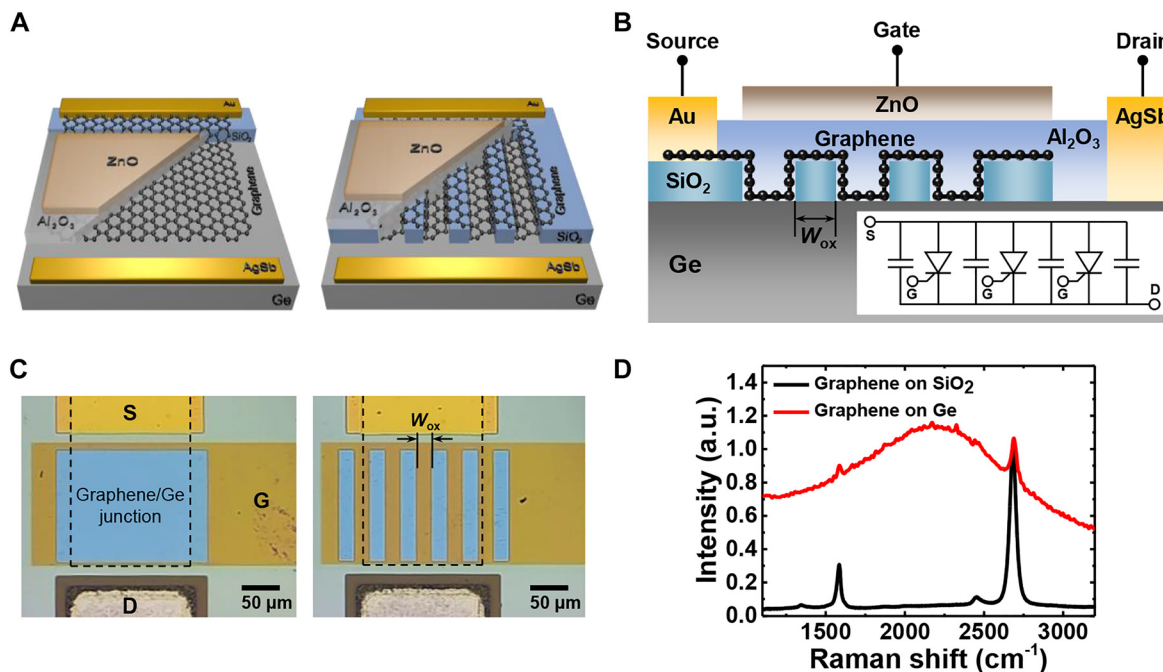

Figure 1: (A) Schematic diagrams of the single (left) and split (right) active junction structure of the gate-controlled graphene/Ge Schottky junction photodetector. (B) Cross-sectional schematic of a split active junction device. W_{ox} represents the width of the interdigitated oxide layer, and four devices ($W_{ox} = 0$, 10, 20, or 30 μm) were fabricated. Inset: equivalent circuit, where the capacitors are connected in parallel with the gate-controlled Schottky diodes. (C) Optical images of fabricated single (left) and split (right) active junction devices. Black dashed rectangle: graphene area. (D) Raman spectrum of monolayer graphene on SiO$_2$ and Ge substrate.

process. For the drain electrode, a 45-nm-thick AgSb alloy (Ag with 1% Sb) was formed on the Ge region using a thermal evaporator and a lift-off process, followed by rapid thermal annealing (RTA) for 5 min in a N_2 atmosphere at 450 °C. After the formation of the AgSb drain contact, the contact resistance of the AgSb electrode was measured using the circular transfer length method [28]. The measured specific contact resistivity was $\rho_c = 4.7 \times 10^{-7}$ Ω cm^2 (refer to Figure S1 in the Supporting Information). This is a relatively low contact resistance for moderately-doped n-type Ge, considering that highly doped n-Ge ($N_D > 1 \times 10^{19}$ cm^{-3}) was used to obtain a low specific contact resistivity of $\rho_c = 1.68 \times 10^{-7}$ Ω cm^2 by using a NiGe ohmic contact [29].

After forming the electrodes, a 50-nm-thick Al_2O_3 layer was deposited at 200 °C using atomic layer deposition (ALD) (Lucida D100, NCD tech) as the gate dielectric. A 50-nm-thick transparent ZnO film was deposited using ALD, and the ZnO top gate was then patterned using photolithography and HCl wet etching. The growth rates of Al_2O_3 and ZnO measured using spectroscopic ellipsometry were ~1 Å and 1.7 Å per cycle, respectively. Finally, passivation annealing was performed at 300 °C under high vacuum conditions for 1 h to remove any remaining water molecules from the interface of graphene and Ge and to densify the Al_2O_3 layer.

The current–voltage (I–V) characteristics of the photodetector were measured using a semiconductor parameter analyzer (Keithley 4200). All characterizations were performed under ambient conditions in air (temperature $T = 300$ K, pressure $P = 1$ atm). The photoresponse characteristics were measured using solid-state laser diodes at wavelengths $\lambda = 520, 850, 1060, 1310, 1550,$ and 1625 nm. For SPCM measurements, a solid-state laser ($\lambda = 1550$ nm) was focused through the objective lens (Olympus LUCPlanFLN, NA = 0.6, 40×) of a microscope and scanned using a two-axis galvanometer scanner. The photocurrent signals were collected using a picoammeter (Keithley 2502) as a function of the laser position. The diffraction-limited spot size at $\lambda = 1550$ nm was ~3.5 μm. The incident light power was monitored using an optical power meter (Newport 1918-C) and a thermopile

sensor (Newport 919P-003-10). Figure S2 in the Supporting Information section provides more information on the experimental setup used to characterize the photoresponsivity.

3 Results and discussion

Figure 2A and B shows the I–V characteristics of the single and split active graphene/Ge Schottky junction photodetectors in the dark and under illumination, respectively. The dark currents of both devices had the characteristics of a typical Schottky junction and were substantially modulated by the gate bias (Figure 2A and B, black lines). In both cases, the rectification ratios increased by more than four orders of magnitude at a drain bias of ±2 V with the top-gate modulation of the Schottky barrier. In addition, the photocurrents, defined as $I_{photo} = I_{illumination} - I_{dark}$, significantly increased at a negative gate bias of –10 V, but were negligible at a positive gate bias of 10 V (Figure 2A and B, red lines). Figure 2C shows the energy band diagrams illustrating the gate modulation mechanism of the Schottky barrier height. The Fermi level of graphene is sensitive to gate bias; thus, the height of the Schottky barrier changes as a function of gate bias. When a negative bias is applied to the gate, the Fermi level of graphene decreases; thereby, increasing the height of the graphene/ Ge Schottky barrier. Moreover, the depletion width in the Ge substrate increases, causing additional band bending and an increase in the hole concentration of graphene [15].
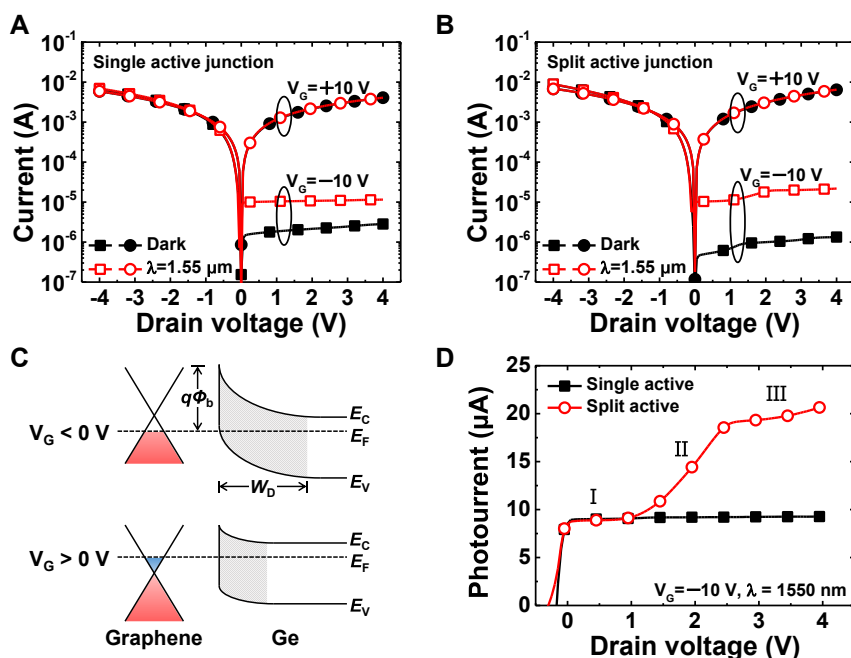

Figure 2: Current–voltage characteristics of the (A) single and (B) split active graphene/ Ge Schottky junction photodetectors in the dark and under illumination. (C) Energy band diagrams of the graphene/Ge Schottky junction with gate-modulation at equilibrium ($V_D = 0$ V). Here, Φ_b, E_C, E_V, E_F, and W_D represent the Schottky barrier height, conduction band edge, valence band edge, Fermi level, and depletion width, respectively. (D) Linear photocurrents for the graphene/Ge Schottky junction photodetectors at $V_G = -10$ V. Photoresponse characteristics were measured at a wavelength of 1550 nm with an incident light power of 10 μW.

In contrast, with a positive gate bias, the Fermi level of graphene shifts upward, and the barrier height decreases; thus, an ohmic-like behavior develops.

Figure 2D shows the photocurrent curves on a linear scale at a negative gate bias of −10 V for single and split active junction photodetectors. The photodetector with a single active region had a nearly constant photocurrent under infrared illumination, regardless of the drain bias. In contrast, the *I*–*V* curve of the photodetector with the split active junction structure had nonlinear characteristics with several linear parts of different slopes, depicted as regions I, II, and III, which correspond to different current-transport mechanisms. Region I corresponds to thermionic emission through the Schottky barrier as the Schottky junction mechanism. In region II, the kink appeared when the applied voltage exceeded 1 V; this region corresponds to the carrier multiplication in Ge owing to the high internal electric field caused by the high drain bias. A high electric field strength could accelerate charge carriers in the

depletion region and result in carrier multiplication, such as impact ionization. This effect causes a nonlinear increase in the current as the applied bias increases. In region III, where the drain bias was higher than 2.5 V, the increase in photocurrent was significantly reduced because the effect of carrier multiplication was suppressed. This trend can be attributed to an increase in non-radiative recombination through deep defect centers or Auger recombination [30, 31].

To further investigate the effect of the split active regions, the spatial distribution of the photocurrents was measured using the SPCM. Figure 3A shows the optical images of the photodetectors with different oxide widths of 0–30 μm. The device was scanned at a size of 3 μm per pixel in a total scanned area of 162 μm × 219 μm. Figure 3B shows the SPCM images for drain biases of 0.5 and 3 V at a gate bias of −10 V in each device. Regardless of the drain bias, photocurrents were higher in the graphene/SiO$_2$/Ge region than in the graphene/Ge region for all devices. In
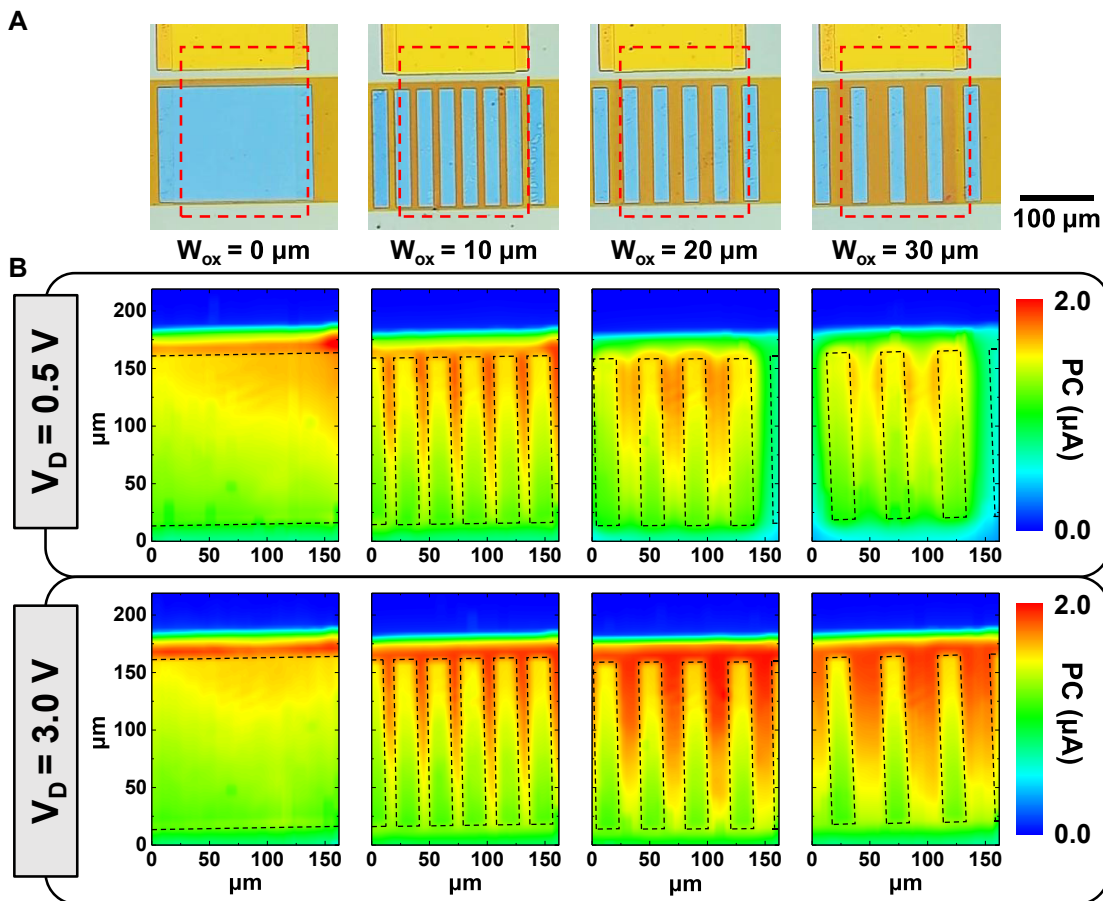

Figure 3: (A) Optical images of the photodetectors with various oxide widths (W_{ox} = 0, 10, 20, or 30 μm). Red dashed line: area in which scanning photocurrent microscopy (SPCM) was measured. (B) SPCM images of the scanned area measured by a 1550 nm laser of 10 μW. Photocurrent measured at V_D = 0.5 V (above) and 3 V (below) under V_G = −10 V, respectively. Black dashed rectangle: graphene/Ge junctions. The scale of the photocurrents is the same for all measurements.

particular, a remarkable photoresponse was observed in the graphene/SiO$_2$/Ge regions at a drain bias of 3 V. These results suggest that a large photocurrent is generated in the graphene/SiO$_2$/Ge regions owing to the self-gating effect of the graphene/SiO$_2$/Ge capacitors by the drain bias. These phenomena can be explained by the formation of an inversion layer underneath the graphene/SiO$_2$/Ge structure of the devices [20, 21]. In addition, the formation of an inversion layer increases the concentration of minority carriers near the surface, thereby reducing surface recombination at the oxide–semiconductor interface and consequently improving the photocurrent [32].

Figure 4A illustrates the dark current trends of split active junction photodetectors with different oxide region widths measured at drain biases of 0.5 and 3.0 V under a gate bias of –10 V. As the oxide width increased, that is, as the area of the graphene/Ge junction decreased, the dark currents were suppressed for both drain biases. This result is consistent with the classical Schottky junction theory, which states that the reverse leakage current caused by the diffusion of minority carriers is proportional to the area of the Schottky junction [33].

To quantitatively analyze the performance of the photodetector, the responsivity R, external quantum efficiency EQE, and specific detectivity D^* were calculated using the following equations:

$$R = \frac{I_{ph}}{P_{in}}, \quad EQE = R\frac{hc}{q\lambda}, \quad D^* = R\sqrt{\frac{A}{2qI_{dark}}}, \tag{1}$$

where I_{ph} is the photocurrent, P_{in} is the power of the incident light, h is Planck's constant, c is the speed of light in a vacuum, q is the elementary electric charge, λ is the wavelength of the light, I_{dark} is the dark current, and A is the area of the device. The photosensitive area was calculated to be 160 μm × 165 μm for all devices, including the areas of the graphene/Ge region and the graphene/SiO$_2$/Ge region. The performance trends shown in Figure 4B and C suggest that the split active junction photodetector with an oxide width of 20 μm is the most efficiently designed structure, which has the highest responsivity and detectivity. In particular, the responsivity and specific detectivity drastically increased at a drain bias of 3 V, resulting from the formation of the inversion layer in the graphene/SiO$_2$/Ge region. As a result, at a gate bias of –10 V and a drain bias of 3 V, a responsivity of 2.02 A W^{-1} with an EQE of 162% and specific detectivity of 5.28 × 10^{10} Jones were achieved. The reduced responsivity in devices with oxide widths greater than 20 μm suggests that the photocarriers generated in the graphene/SiO$_2$/Ge regions are farther away from the graphene/Ge junction, resulting in a weaker lateral electric field and consequently difficult to extract into the graphene/Ge junction before carrier recombination. Figure 4D shows the spectral responsivity and EQE of an optimized photodetector in the range of 520–1625 nm at a constant light intensity of 25 μW. The photodetector has peak sensitivity at a wavelength of 1310 nm, which is attributed to the intrinsic light absorption at germanium.

A numerical simulation of the local electric field was performed to better understand the physical mechanisms of the enhanced photocurrents in the split active junction of the photodetectors. An ideal Schottky junction was modeled in two dimensions under a reverse bias of 4 V,
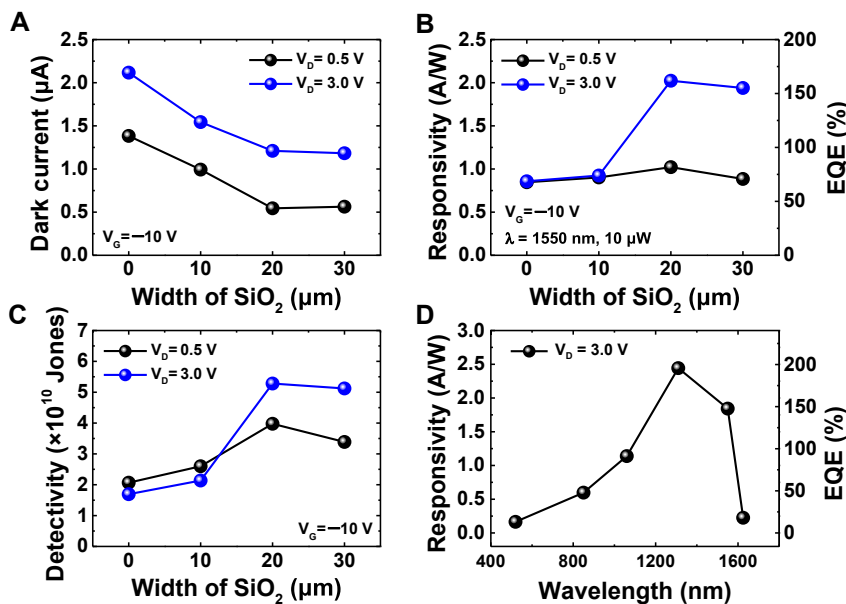

Figure 4: (A–C) Performance comparison of split active junction photodetectors as a function of SiO$_2$ width: (A) dark current measured at V_D = 0.5 and 3 V under V_G = –10 V; (B) responsivity (left axis) with calculated EQE (right axis); (C) specific detectivity measured at a wavelength of 1550 nm with an incident light power of 10 μW. (D) Wavelength-dependent responsivity (left axis) and EQE (right axis) of the split active junction photodetector measured at a fixed light intensity of 25 μW.

where graphene with a work function of 4.5 eV was placed on the top of a 100-nm-thick SiO_2 patterned to a width of 20 μm on an n-type Ge substrate with a doping concentration of 4.7×10^{15} cm^{-3}. Figure 5A shows the simulated electric field strength and direction inside the Ge substrate, and the line profiles of the x- and y-components of the electric field (E_x and E_y) along 10 nm below the Ge surface. The electric field was strengthened at the edges of the SiO_2 region. In particular, E_x was significantly enhanced at the edges of the SiO_2 region compared to the middle, resulting in an in-plane electric field outside the SiO_2 region. The direction of this electric field caused the photogenerated carriers to migrate from the edge of the graphene/SiO_2/Ge region to the graphene/Ge junction. In contrast, the electric field in the middle of the SiO_2 region was dominated by an almost constant E_y, whereas E_x was negligible. This electric field distribution induced a diffusion process rather than a drift process of photocarriers generated in the middle of the graphene/SiO_2/Ge region; the detailed process will be described later. These simulation results demonstrate that the origin of the enhanced photocurrent is caused by a series of transport processes, in which photogenerated holes in Ge below the SiO_2 drift and diffuse into the Ge

window region. First, the photogenerated holes preferentially travel vertically and accumulate at the SiO_2/Ge interface by E_y. Thereafter, because E_x is weak, the holes diffuse horizontally to the edge of the graphene/SiO_2/Ge region. Finally, the holes are accelerated by the strong electric field in the transition region between graphene/SiO_2/Ge and graphene/Ge and collected into the graphene/Ge Schottky region.

The schematic energy band diagrams derived from this understanding are shown in Figure 5B and C as a function of depth from the Ge surface at the edge of the graphene/SiO_2/Ge region and the middle of the graphene/Ge junction, respectively. Figure 5D shows a lateral energy band diagram along the Ge surface. The accumulated hole layer on the Ge surface caused energy band misalignment between the graphene/SiO_2/Ge region and the graphene/Ge junction. The photogenerated minority charge carriers were extracted into the graphene channel because of the lateral electric field in the transition region, and carrier multiplication might occur under a strong electric field greater than the breakdown electric field of 10^5 V cm^{-1} for Ge [34, 35]. The misalignment of the energy band and enhancement of the electric field in the transition region
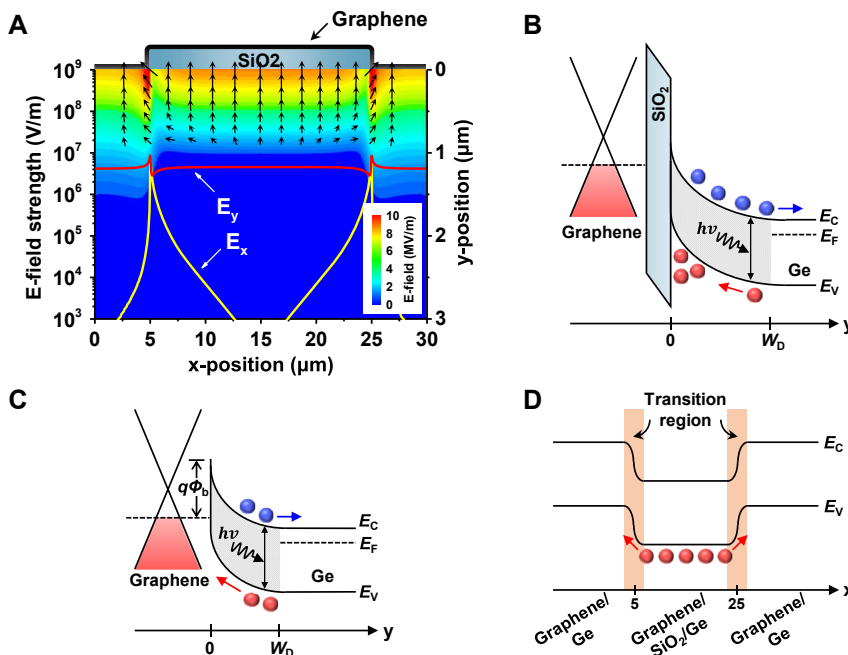

Figure 5: (A) Two-dimensional numerical simulation of the electric field between graphene/Ge and graphene/SiO_2/Ge region under reverse bias condition ($V_D = 4$ V). Line profiles exhibit the x- and y-components of the electric field (E_x and E_y) 10 nm below the Ge surface along the x-direction. Black arrow: the electric field strength and direction in the Ge substrate. Schematic energy band diagrams of (B) the edge of the graphene/SiO_2/Ge region and (C) the middle of the graphene/Ge Schottky junction along the y-direction. (D) Lateral band diagram along the Ge surface. Blue and red circle: photogenerated electron and hole in Ge, respectively. Here, Φ_b, E_C, E_V, E_F, and W_D represent the Schottky barrier height, conduction band edge, valence band edge, Fermi level, and depletion width, respectively.

qualitatively indicate that strong energy band bending in Ge significantly affects the transport of photogenerated carriers in the split active junction.

Figure 6A illustrates a scheme that depicts the transport mechanisms of photogenerated carriers, according to the band diagrams derived from the simulation results. Although the photogenerated holes in the graphene/Ge Schottky region were immediately extracted through the graphene channel, the photogenerated holes at the edge of the graphene/SiO$_2$/Ge region must travel the distance to the graphene/Ge Schottky junction. In contrast, the transport of photogenerated holes in the middle of the graphene/SiO$_2$/Ge region was dominated by ambipolar diffusion. Figure 6B shows the diffusion process in which some of the electron–hole pairs recombine along the SiO$_2$/Ge interface. The photocurrent continuously decreased as the photogenerated carriers diffused along the SiO$_2$/Ge interface because carrier recombination was increased by the interface states along the interface.

Figure 6C shows the drain bias-dependent photocurrent map at a gate bias of –10 V in the split active junction device with an oxide width of 40 μm. As the drain bias increased, the photocurrent remarkably increased in the graphene/SiO$_2$/Ge region, and the photocurrent was greatest at the edge of the graphene/SiO$_2$/Ge region. Under a high drain bias, the depletion region widened owing to the increased

band bending in the transition region, resulting in more photocarrier generation. As a result, the photogenerated carriers could be extracted more efficiently at the edge of the graphene/SiO$_2$/Ge region compared to the middle of the graphene/Ge Schottky junction.

A detailed analysis of the position-dependent photocurrent line profile was performed using the SPCM, as shown in Figure 6D. The measured photocurrent I_{ph} in the graphene/SiO$_2$/Ge region as a function of position x is described as the number of excess carriers collected by the graphene channels. The diffusion length of the photogenerated carriers was calculated directly from the photocurrent decay for different drain biases of 1 and 3 V. In the absence of an external electric field, the collected photocurrent analytically leads to a simple one-dimensional exponential function for $x > 0$ as follows [36, 37]:

$$I_{ph} = \frac{qG}{2} \exp\left(-\frac{x}{L_d}\right), \tag{2}$$

where I_{ph} is the photocurrent, q is the elementary electric charge, G is the carrier generation rate, and $L_d = (D_p \tau_p)^{1/2}$ is the diffusion length with the diffusion coefficient of hole D_p and the lifetime of hole τ_p. The decay profile of the photocurrent followed a simple exponential function with diffusion lengths L_d = 10.9 and 19.2 μm at drain biases of 1 and 3 V, respectively. The diffusion length increased at higher
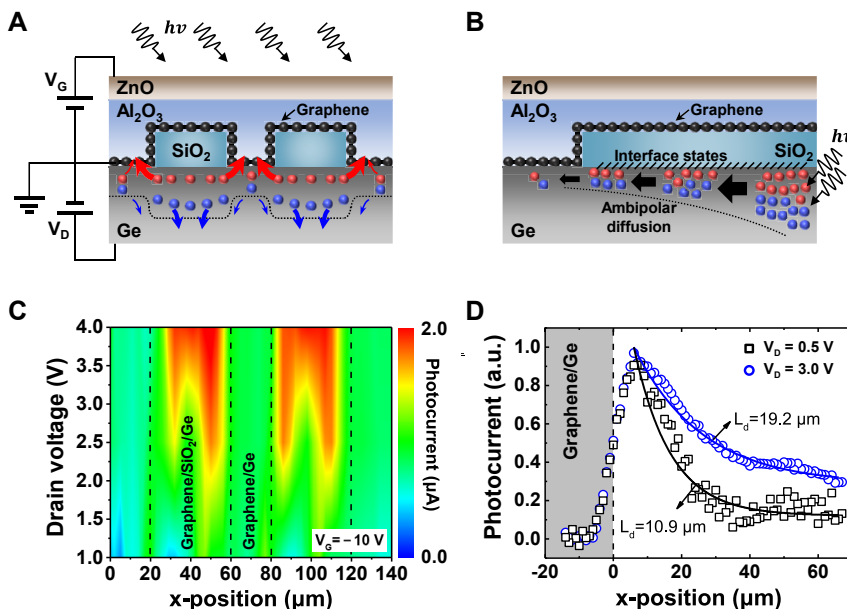

Figure 6: (A) Schematic diagram of the carrier generation, extraction, and collection mechanisms in a split active junction photodetector under illumination. Blue and red circle: photogenerated electron and hole in Ge, respectively. (B) Schematic diagram of the ambipolar diffusion along the SiO$_2$/Ge interface. The interface states are presented at the interface between SiO$_2$ and Ge. (C) Photocurrent map as a function of V_D from 1 to 4 V under V_G = –10 V at incident light power of 10 μW. Black dashed line: transition region. (D) Photocurrent decay profile as a function of the incident light position in the graphene/SiO$_2$/Ge region measured at V_D = 0.5 and 3 V under V_G = –10 V. Solid lines are a fit to the data, and the diffusion lengths are 10.9 and 19.2 μm at V_D = 0.5 and 3 V, respectively.

drain biases, which was consistent with the expectation that the strong band bending in the transition region affected the transport of photogenerated carriers. This correlation suggests that the split active junction structure should be designed with appropriate dimensions in consideration of the internal electric field according to the thickness of the oxide or the operating voltage to optimize the photodetector.

4 Conclusions

The responsivity of the graphene/Ge photodetector increased with a reduced dark current by splitting the active region into a graphene/SiO_2/Ge structure to increase the EQE. These changes increased the EQE to 162%, the responsivity to 2.02 A W^{-1}, and the specific detectivity to 5.28×10^{10} Jones. A simulation study indicated that a strong internal electric field was formed beneath the graphene/SiO_2/Ge regions and helped to generate and efficiently collect photogenerated carriers. Advances in the structural understanding of these devices without additional processes provide a promising approach for future high-performance optoelectronics.

References

[1] X. Li, H. Zhu, K. Wang, et al., "Graphene-on-silicon Schottky junction solar cells," Adv. Mater., vol. 22, no. 25, pp. 2743–2748, 2010.

[2] L. Zhang, L. Fan, Z. Li, et al., "Graphene-CdSe nanobelt solar cells with tunable configurations," Nano Res., vol. 4, no. 9, pp. 891–900, 2011.

[3] G. Konstantatos, M. Badioli, L. Gaudreau, et al., "Hybrid graphene–quantum dot phototransistors with ultrahigh gain," Nat. Nanotechnol., vol. 7, no. 6, pp. 363–368, 2012.

[4] Y. An, A. Behnam, E. Pop, and A. Ural, "Metal-semiconductor-metal photodetectors based on graphene/p-type silicon Schottky junctions," Appl. Phys. Lett., vol. 102, no. 1, p. 013110, 2013.

[5] X. An, F. Liu, Y. J. Jung, and S. Kar, "Tunable graphene–silicon heterojunctions for ultrasensitive photodetection," Nano Lett., vol. 13, no. 3, pp. 909–916, 2013.

[6] P. Lv, X. Zhang, X. Zhang, W. Deng, and J. Jie, "High-sensitivity and fast-response graphene/crystalline silicon Schottky junction-based near-IR photodetectors," IEEE Electron. Device Lett., vol. 34, no. 10, pp. 1337–1339, 2013.

[7] F. Liu and S. Kar, "Quantum carrier reinvestment-induced ultrahigh and broadband photocurrent responses in graphene–silicon junctions," ACS Nano, vol. 8, no. 10, pp. 10270–10279, 2014.

[8] J. Miao, W. Hu, N. Guo, et al., "High-responsivity graphene/InAs nanowire heterojunction near-infrared photodetectors with distinct photocurrent on/off ratios," Small, vol. 11, no. 8, pp. 936–942, 2015.

[9] S. Kim, T. H. Seo, M. J. Kim, K. M. Song, E.-K. Suh, and H. Kim, "Graphene-GaN Schottky diodes," Nano Res., vol. 8, no. 4, pp. 1327–1338, 2015.

[10] W. Zhang, C.-P. Chuu, J.-K. Huang, et al., "Ultrahigh-gain photodetectors based on atomically thin graphene-MoS₂ heterostructures," Sci. Rep., vol. 4, no. 1, p. 3826, 2015.

[11] Z. Chen, Z. Cheng, J. Wang, et al., "High responsivity, broadband, and fast graphene/silicon photodetector in photoconductor mode," Adv. Opt. Mater., vol. 3, no. 9, pp. 1207–1214, 2015.

[12] K. E. Chang, T. J. Yoo, C. Kim, et al., "Gate-controlled graphene–silicon Schottky junction photodetector," Small, vol. 14, no. 28, p. 1801182, 2018.

[13] L.-H. Zeng, M.-Z. Wang, H. Hu, et al., "Monolayer graphene/germanium Schottky junction as high-performance self-driven infrared light photodetector," ACS Appl. Mater. Interfaces, vol. 5, no. 19, pp. 9362–9366, 2013.

[14] F. Yang, H. Cong, K. Yu, et al., "Ultrathin broadband germanium–graphene hybrid photodetector with high performance," ACS Appl. Mater. Interfaces, vol. 9, no. 15, pp. 13422–13429, 2017.

[15] K. E. Chang, C. Kim, T. J. Yoo, et al., "High-responsivity near-infrared photodetector using gate-modulated graphene/germanium Schottky junction," Adv. Electron. Mater., vol. 5, no. 6, p. 1800957, 2019.

[16] S. Srisonphan, "Hybrid graphene–Si-based nanoscale vacuum field effect phototransistors," ACS Photonics, vol. 3, no. 10, pp. 1799–1808, 2016.

[17] A. Di Bartolomeo, F. Giubileo, G. Luongo, et al., "Tunable Schottky barrier and high responsivity in graphene/Si-nanotip optoelectronic device," 2D Mater., vol. 4, no. 1, p. 015024, 2016.

[18] A. Di Bartolomeo, G. Luongo, F. Giubileo, et al., "Hybrid graphene/silicon Schottky photodiode with intrinsic gating effect," 2D Mater., vol. 4, no. 2, p. 025075, 2017.

[19] S. Riazimehr, S. Kataria, R. Bornemann, et al., "High photocurrent in gated graphene–silicon hybrid photodiodes," ACS Photonics, vol. 4, no. 6, pp. 1506–1514, 2017.

[20] G. Luongo, F. Giubileo, L. Genovese, L. Iemmo, N. Martucciello, and A. Di Bartolomeo, "I-V and C-V characterization of a high-responsivity graphene/silicon photodiode with embedded MOS capacitor," Nanomaterials, vol. 7, no. 7, p. 158, 2017.

[21] S. Riazimehr, S. Kataria, J. M. Gonzalez-Medina, et al., "High responsivity and quantum efficiency of graphene/silicon photodiodes achieved by interdigitating Schottky and gated regions," ACS Photonics, vol. 6, no. 1, pp. 107–115, 2019.

[22] N. Unsuree, H. Selvi, M. G. Crabb, J. A. Alanis, P. Parkinson, and T. J. Echtermeyer, "Visible and infrared photocurrent enhancement in a graphene-silicon Schottky photodetector through surface-states and electric field engineering," 2D Mater., vol. 6, no. 4, p. 041004, 2019.

[23] G. Luongo, A. Grillo, F. Giubileo, et al., "Graphene Schottky junction on pillar patterned silicon substrate," Nanomaterials, vol. 9, no. 5, p. 659, 2019.

[24] C. Kim, T. J. Yoo, K. E. Chang, M. G. Kwon, H. J. Hwang, and B. H. Lee, "Highly responsive near-infrared photodetector with low dark current using graphene/germanium Schottky junction with Al_2O_3 interfacial layer," Nanophotonics, vol. 10, no. 5, p. 1573, 2021.

[25] Z. Zhao, C. Xu, L. Niu, X. Zhang, and F. Zhang, "Recent progress on broadband organic photodetectors and their applications," Laser Photon. Rev., vol. 14, no. 11, p. 2000262, 2020.

[26] B. Onsia, M. Caymax, T. Conard, et al., "On the application of a thin ozone based wet chemical oxide as an interface for ALD high-k deposition," Solid State Phenom., vol. 103, no. 104, pp. 19–22, 2005.

[27] S. R. Amy, Y. J. Chabal, F. Amy, A. Kahn, C. Krugg, and P. Kirsch, "Wet chemical cleaning of germanium surfaces for growth of high-k dielectrics," MRS Proc., vol. 917, 2006, Art. no. 0917-E01-05.

[28] D. C. S. Dumas, K. Gallacher, R. Millar, et al., "Silver antimony ohmic contacts to moderately doped n-type germanium," Appl. Phys. Lett., vol. 104, no. 16, p. 162101, 2014.

[29] K. F. Gallacher, P. Velha, D. J. Paul, I. Maclaren, M. Myronov, and D. R. Leadly, "Low specific ohmic contacts to n-type germanium using a low temperature NiGe process," ECS Trans., vol. 50, no. 9, pp. 1081–1084, 2013.

[30] S. Lei, F. Wen, L. Ge, et al., "An atomically layered InSe avalanche photodetector," Nano Lett., vol. 15, no. 5, pp. 3048–3055, 2015.

[31] V. P. Sirkeli, O. Yilmazoglu, A. S. Hajo, et al., "Enhanced responsivity of ZnSe-based metal-semiconductor-metal near-ultraviolet photodetector via impact ionization," Phys. Status Solidi Rapid Res. Lett., vol. 12, no. 2, p. 1700418, 2018.

[32] W. J. Royea, D. J. Michalak, and N. S. Lewis, "Role of inversion layer formation in producing low effective surface recombination velocities at Si/liquid contacts," Appl. Phys. Lett., vol. 77, no. 16, pp. 2566–2568, 2000.

[33] C. R. Crowell and S. M. Sze, "Current transport in metal-semiconductor barriers," Solid State Electron., vol. 9, no. 11, pp. 1035–1048, 1966.

[34] T. Mikawa, S. Kagawa, T. Kaneda, Y. Toyama, and O. Mikami, "Crystal orientation dependence of ionization rates in germanium," Appl. Phys. Lett., vol. 37, no. 4, pp. 387–389, 1980.

[35] A. Kyuregyan and S. N. Yurkov, "Room-temperature avalanche breakdown voltages of p-n-junctions made of Si, Ge, SiC, GaAs, GaP, and InP," Sov. Phys. Semiconduct., vol. 23, pp. 1126–1131, 1989.

[36] J. Navas, E. Guillén, R. Alcántara, et al., "Direct estimation of the electron diffusion length in dye-sensitized solar cells," J. Phys. Chem. Lett., vol. 2, no. 9, pp. 1045–1050, 2011.

[37] J.-K. Park, J.-C. Kang, S. Y. Kim, et al., "Diffusion length in nanoporous photoelectrodes of dye-sensitized solar cells under operating conditions measured by photocurrent microscopy," J. Phys. Chem. Lett., vol. 3, no. 23, pp. 3632–3638, 2012.

Supplementary Material: The online version of this article offers supplementary material (https://doi.org/10.1515/nanoph-2021-0738).